

How Can Active Region Plasma Escape into the Solar Wind from Below a Closed Helmet Streamer?

C.H. Mandrini · F.A. Nuevo · A.M. Vásquez ·
P. Démoulin · L. van Driel-Gesztelyi · D. Baker ·
J.L. Culhane · G.D. Cristiani · M. Pick

Received: 6 March 2014 / Accepted: 24 July 2014 / Published online: 21 August 2014
© Springer Science+Business Media Dordrecht 2014

Abstract Recent studies show that active-region (AR) upflowing plasma, observed by the *EUV-Imaging Spectrometer* (EIS) onboard *Hinode*, can gain access to open-field lines and be released into the solar wind (SW) *via* magnetic-interchange reconnection at magnetic null-points in pseudo-streamer configurations. When only one bipolar AR is present on the Sun and is fully covered by the separatrix of a streamer, such as AR 10978 in December 2007, it seems unlikely that the upflowing AR plasma can find its way into the slow SW. However, signatures of plasma with AR composition have been found at 1 AU by Culhane *et al.* (*Solar Phys.* **289**, 3799, 2014) that apparently originated west of AR 10978. We present a detailed topology analysis of AR 10978 and the surrounding large-scale corona based on a potential-field source-surface (PFSS) model. Our study shows that it is possible for the AR plasma to move around the streamer separatrix and be released into the SW *via* magnetic reconnection, which occurs in at least two main steps. We analyse data from the *Nançay Radioheliograph* (NRH) in a search for evidence of the chain of magnetic reconnections that we propose. We find a noise storm above the AR and several varying sources at 150.9 MHz. Their locations suggest that they might be associated with particles accelerated during the first-step reconnection process at a null point well outside of the AR. We find no evidence of the second reconnection step in the radio data, however. Our results demonstrate that even

C.H. Mandrini (✉) · F.A. Nuevo · A.M. Vásquez · G.D. Cristiani
Instituto de Astronomía y Física del Espacio (IAFE), CONICET-UBA, Buenos Aires, Argentina
e-mail: mandrini@iafe.uba.ar

C.H. Mandrini · F.A. Nuevo · A.M. Vásquez · G.D. Cristiani
Facultad de Ciencias Exactas y Naturales (FCEN), UBA, Buenos Aires, Argentina

P. Démoulin · L. van Driel-Gesztelyi · M. Pick
Observatoire de Paris, LESIA, UMR 8109 (CNRS), 92195 Meudon Principal Cedex, France

L. van Driel-Gesztelyi · D. Baker · J.L. Culhane
UCL-Mullard Space Science Laboratory, Holmbury St. Mary, Dorking, Surrey, RH5 6NT, UK

L. van Driel-Gesztelyi
Konkoly Observatory, Research Centre for Astronomy and Earth Sciences, Hungarian Academy of Sciences, Budapest, Hungary

when it appears highly improbable for the AR plasma to reach the SW, indirect channels involving a sequence of reconnections can make it possible.

Keywords Active regions · Magnetic fields · Magnetic extrapolations · Corona active · Solar wind · Radio Bursts · Type I · Radio emission · Quiet

1. Introduction

Parker's seminal work (Parker, 1958, 1963) postulated that the million-degree high-conductivity solar corona must be in continuous expansion. This laid the foundations of a new branch of solar-heliospheric physics: the study of the origin and characteristics of the solar wind (SW). The steady, faster component of the SW originates from large coronal holes (CHs), while small CHs produce a slower wind (Miralles *et al.*, 2001, 2004; Neugebauer *et al.*, 2002). Additionally, a much more variable and slow component of the SW is frequently associated with coronal streamers. In bipolar streamers, this slow wind is usually observed at 1 AU around the heliospheric current sheet (HCS). Most importantly, while the fast steady wind shows a stable chemical composition, with values similar to those at the photospheric level (von Steiger, Geiss, and Gloeckler, 1997, 2001; Zurbuchen *et al.*, 1999, 2002), the slow wind is characterized by variable abundances, with values typical of closed-field active regions. Such abundances are mainly dependent on the first ionization potential (FIP) of the element considered, with the high-FIP elements being typically more enhanced than low-FIP elements in a wide range from two to ten, with typical values for ARs between three to five (*e.g.* Feldman and Widing, 2003; Zurbuchen and von Steiger, 2006; Brooks and Warren, 2011). There is still no clear consensus of opinion from which location the slow unsteady wind originates, however.

The scenarios proposed for the origin of the slow wind can be divided into five categories:

- i) The slow wind originates from the boundary of CHs (Suess, 1979; Wang and Sheeley, 1990; Cranmer, van Ballegooijen, and Edgar, 2007). In these models, the terminal SW speed is inversely related to the expansion factor of the open-field lines, which in turn depends on the height of heat deposition by magnetohydrodynamic (MHD) waves. The relationship is such that for lower deposition heights the terminal SW speed is lower (Holzer and Leer, 1980). These models cannot explain the variable FIP-biased composition of the slow wind, however.
- ii) The interchange reconnection model (Fisk, Schwadron, and Zurbuchen, 1998; Fisk, 2003; Fisk and Zhao, 2009) suggests that closed loops and open-field lines are both present over quiet-Sun areas and that the slow wind originates from magnetic reconnection between them, induced by a continuously changing magnetic carpet. This model naturally explains the dynamic properties of the slow wind, but Antiochos *et al.* (2007) doubted that mixing of open and closed fields over quiet-Sun regions is possible, based on Lorentz-force-balance considerations.
- iii) The slow wind originates at streamer tops. Closed flux may expand and open up, and interchange reconnection can take place at these locations between open- and closed-field lines (Wang *et al.*, 2000). In spite of extensive supporting observational evidence, the narrowness of the latitudinal extent of the reconnecting region implies that other mechanisms also need to be at work to match the much broader latitudinal extent over which the slow wind is observed (McComas *et al.*, 1998).

- iv) The most recent, so-called separatrix-web (S-Web) model of slow-wind formation was proposed jointly by Antiochos *et al.* (2011), Titov *et al.* (2011), and Linker *et al.* (2011) and was further developed by Antiochos *et al.* (2012). Their model is based on the “uniqueness conjecture”, discussed by Antiochos *et al.* (2007), which states that “any unipolar region on the photosphere can contain at most one CH”. This implies that multiple CHs are connected. The connecting corridors are thought to be thin, occasionally infinitely thin. As these corridors represent drastic change of magnetic connectivity in the corona, they are, in fact, quasi-separatrix layers (QSLs; Démoulin *et al.*, 1996), which might include separatrices (Masson *et al.*, 2009). The slow wind is suggested to originate along these corridors as they continuously open and close by reconnection.
- v) Morgan, Jeska, and Leonard (2013) have found that the expansion of closed AR loops, discovered by Uchida *et al.* (1992), continues well above the source surface at $2.5 R_{\odot}$ up to $12 R_{\odot}$. However, doubts have been raised by Gopalswamy *et al.* (2013) about how high charge states found in the slow wind can be generated by steadily expanding AR loops without requiring magnetic reconnection. It is also difficult to understand in this scenario why occasionally slow-wind signatures only appear on one side of the heliospheric plasma sheet (HPS), because the expansion of loops would imply symmetrical slow-wind streams on both sides.

A different approach was taken by the high-resolution spectroscopy community. Since the discovery of persistent hot plasma upflows from the edges of solar active regions (ARs) by the *Hinode*/X-ray Telescope (XRT; Sakao *et al.*, 2007) and the *EUV-Imaging Spectrometer* (EIS; Harra *et al.*, 2008), it has been suspected that these upflows are in fact outflows that contribute to the slow wind. Baker *et al.* (2009) demonstrated that upflows occur at specific locations of an AR magnetic topology, along QSLs where current sheets form and magnetic reconnection takes place. A pressure gradient, resulting from reconnection between loops of different density, was proposed as a driver of the plasma upflows. Using potential-field extrapolations, Del Zanna *et al.* (2011) linked the upflows of an AR to a high-altitude coronal null point in a pseudo- (or unipolar) streamer configuration, where interchange reconnection can take place, creating a steep pressure gradient and a rarefaction wave in the reconnected loops (Bradshaw, Aulanier, and Del Zanna, 2011). As separatrices and nulls are part of the more general QSL concept, the results of Baker *et al.* (2009) and Del Zanna *et al.* (2011) are not contradictory, and they both highlight the key role of the magnetic-field topology and magnetic reconnection in the generation of AR plasma upflows. However, the specific manner in which the plasma upflows of an AR can find their way into the solar wind was, and still is, a key open issue.

Brooks and Warren (2011, 2012) have determined the FIP bias in AR outflows using *Hinode*/EIS data and found matching values in the slow wind observed with the *Advanced Composition Explorer* (ACE) three days later, which is a promising result. Their work supports the existence of a physical link between the plasma outflows in the AR and the slow-wind stream. This connection has been established by van Driel-Gesztelyi *et al.* (2012) through the use of coronal and *in-situ* observations, combined with magnetic modelling. They analysed a complex of two active regions flanked by two low-latitude CHs of opposite magnetic polarity observed between 2–18 January 2008. Linear force-free (LFF) magnetic-field extrapolations of the two ARs confirmed that their plasma outflows are co-spatial with the locations of QSLs, including the separatrix of a magnetic null-point. Complementarily, a global potential-field source-surface (PFSS) model indicated that the smaller AR was only partially covered by a large closed-field streamer. At the null point, present above this AR, interchange reconnection between closed high-density magnetic loops of the small AR and

open evacuated field lines of the neighbouring CH could take place. The resulting pressure gradient led to upflows along the reconnected open-field lines, and downflows along the newly created closed loops, as proposed by Baker *et al.* (2009) and modelled by Bradshaw, Aulanier, and Del Zanna (2011). Using ACE data, van Driel-Gesztelyi *et al.* (2012) showed that the temperature [T], velocity [v], and ion abundances observed in the corresponding slow-wind streams were related to this small parent AR.

In the example analysed by van Driel-Gesztelyi *et al.* (2012), the presence of two bipolar ARs creates a quadrupolar magnetic configuration in which a high-altitude null point can be present. Under favourable circumstances, the spine of this null and the QSLs that surround it can provide a natural channel for the AR outflows into the slow wind. However, when only one simple bipolar AR is present on the Sun and it is fully covered by the separatrix of a streamer, as in the configuration studied by Brooks and Warren (2011, 2012) in December 2007, the question arises whether it is possible for the plasma from the AR to find its way into the slow SW. Culhane *et al.* (2014) revisited the results of Brooks and Warren (2011, 2012), when the only AR present on the visible disc was NOAA AR 10978. Strong upflows, of up to 50 km s^{-1} , were observed with EIS at both sides of this AR during its disc passage (Bryans, Young, and Doschek, 2010; Brooks and Warren, 2011; Démoulin *et al.*, 2013). Although the AR was fully covered by a large streamer separatrix, Culhane *et al.* (2014) found signatures typical of AR plasma in the presumably associated slow-wind stream, which was asymmetric around the HPS. How can the coronal plasma circumvent this topological obstacle? We intend to answer this question in the following sections.

This article is organised as follows: In Section 2, we briefly describe the photospheric and coronal environment surrounding AR 10978. Section 3 presents a global magnetic-field coronal source-surface model, which we use as the boundary condition for a detailed computation of the magnetic topology of the AR and its surroundings. As a result of our topological analysis, in Section 3.4 we discuss how the AR plasma can escape from below the closed streamer configuration *via* magnetic reconnection occurring in at least two steps. We search for coronal signatures of the two-step reconnection process by analysing data from the *Nançay Radioheliograph* (NRH) (Section 4), which is sensitive to low-energy release processes. Finally, in Section 5, we discuss the implications of our topological analysis for the origin of the unsteady slow SW, and we draw some conclusions.

2. The Magnetic and Coronal Environment of AR 10978

2.1. Global Observations During CR 2064

During Carrington rotation (CR) 2064, AR 10978 was the largest catalogued region on the solar disc. This bipolar region transited the disc from 6 to 19 December 2007 as seen from Earth. It had an average total unsigned magnetic flux of 6.0×10^{22} Mx. Figure 1 shows a *Michelson Doppler Imager* (MDI; Scherrer *et al.*, 1995) synoptic map in which AR 10978 is isolated, with only a few other minor regions visible at some distance. The projection on the solar surface of the polarity inversion line (PIL) at $2.5 R_{\odot}$ is shown overlying the synoptic map. In passing over AR 10978, the projection of the PIL roughly agrees with the magnetic inversion line of this AR. Two unipolar areas of opposite polarity, corresponding to two CHs west and east of the AR, are indicated as CH1 and CH2 in Figure 1. The locations of the peripheral EIS upflows, which are relevant to our study are shown as well (see, *e.g.*, Démoulin *et al.*, 2013).

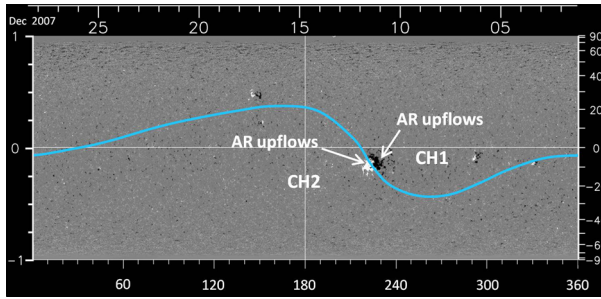
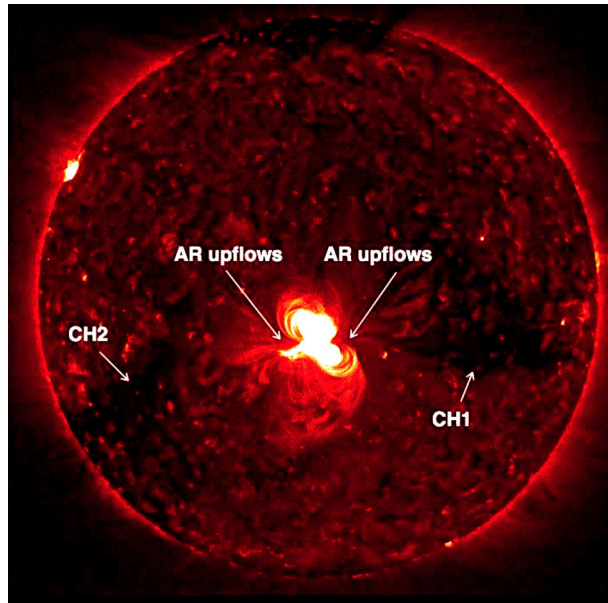


Figure 1 MDI synoptic magnetogram for CR 2064. The horizontal axis indicates the Carrington longitude, the vertical axis on the right corresponds to the Carrington latitude, while that on the left refers to its sine. The thick light-blue line overlying the figure is the projection on the disc of the inversion line at $2.5 R_{\odot}$ computed using the NSO/GONG PFSS model. In passing over the AR, this projection roughly aligns with the main polarity-inversion line of AR 10978. The CHs at both sides of the AR are indicated, as well as the sites of the most prominent upflows observed by EIS. For all figures showing magnetic-field data, white (black) corresponds to positive (negative) field values.

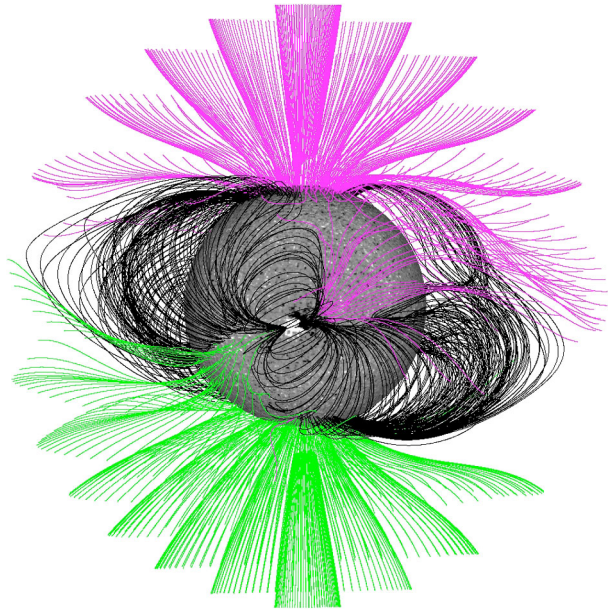
Figure 2 *Hinode*/XRT image showing the hot coronal environment around AR 10978. The image corresponds to the central meridian passage (CMP) of the AR, on 12 December 2007. Two CHs, indicated by arrows, are seen flanking the region, which is the only sizable bright feature on the solar disc. The locations of the main upflows observed by EIS are also indicated by arrows.



The hot coronal environment around AR 10978 is revealed by the X-ray image shown in Figure 2. The two CHs are clearly seen as dim regions at both sides of the AR, which is the only significant bright feature on the disc.

AR 10978 was numbered as AR 10980 during the next Carrington rotation (CR 2065). The comparison of the photospheric environment of these two recurrences of the same AR reveals some differences. Although a few small bipoles emerged during the disc transit of AR 10978, they did not alter its strongly bipolar configuration. On the other hand, AR 10980, while being bipolar and already in its decay phase, was closely followed by a spotless bipolar region that appeared at the eastern limb on 3 January 2008 (van Driel-Gesztelyi *et al.*, 2012).

Figure 3 PFSS model of CR 2064 with AR 10978 at CMP (Carrington longitude 228°). The AR lies completely below the streamer belt and open-field lines of the two CHs are seen at both of its flanks. The field-line colour convention is such that black indicates closed lines and pink (green) corresponds to open lines anchored in the negative-polarity (positive-polarity) field.



The two regions coupled, forming a quadrupolar magnetic configuration. Both AR 10978 (CR 2064) and AR 10980 and its coupled small region (CR 2065) were flanked by CHs and remained stable during their disc transits. A series of C-class X-ray flares occurred in AR 10978, at a rate of two *per* day, after 13 December and until its disappearance behind the western limb. These flaring episodes are related to the emergence of small weak bipoles at both sides of the main negative polarity (see Figure 1 in Démoulin *et al.*, 2013). Only one C-class flare occurred in AR 10980 on 7 January 2008 with an associated small-scale coronal mass ejection (CME) (see Foullon *et al.*, 2011).

2.2. The Global Field Model of CR 2064

The global coronal magnetic field of CR 2064 is modelled using a PFSS approach. These models assume a current-free coronal field with an observationally prescribed and/or modelled boundary condition at the photosphere. PFSS models assume that the field becomes purely radial at a given height called the source surface: a free parameter usually set to the value $2.5 R_{\odot}$. The PFSS model used in this article (see Figure 3) was computed with the Finite Difference Iterative Potential-Field Solver (FDIPS) code described by Tóth, van der Holst, and Huang (2011), using the MDI synoptic magnetogram for CR 2064 as photospheric boundary condition.

Individual full-disc MDI magnetograms are built every 96 minutes. The calibrated photospheric line-of-sight (LOS) field is transformed into the total field strength, assuming the magnetic-field vector is fully radial at the location of the measurement. To construct a synoptic map of the entire solar surface, the field strength is averaged at each grid point from the time series of ≈ 20 magnetograms, which provide data for that grid point in a $\pm(\approx 10^\circ)$ longitudinal range around its CMP. Prior to averaging, the individual magnetograms are interpolated to disc-centre resolution, resulting in a 3600×1080 pixel synoptic map, and differential rotation is accounted for. The axes are linear in Carrington longitude (0.1-degree

intervals) and in sine latitude, so that each synoptic pixel represents the same area on the solar surface. The LOS projection effect severely compromises the measured magnetic data at high latitudes. In the latitude range $\pm 60^\circ$, the synoptic maps only preserve observed data. For higher latitudes, special sets of observations and interpolation schemes are used. Full details concerning the construction of synoptic maps can be found in the MDI web-site (soi.stanford.edu/magnetic/index.html). It is important to keep in mind that synoptic magnetograms are an average description of the magnetic-flux distribution at the solar surface; therefore, they provide a meaningful description for regions that show stability over the averaging period, which is the case for AR 10978.

PFSS models are traditionally computed using a spherical-harmonic decomposition of synoptic magnetograms. These models, if not properly apodized, are characterised by high-frequency artefacts around sharp features. They can also lead to inaccurate and unreliable results when using a grid that is uniform in the sine of the latitude, especially in the polar regions close to the Sun's surface. Alternatively, the FDIPS code, which is freely available from the Center for Space Environment Modeling (CSEM) at the University of Michigan (csem.engin.umich.edu/tools/FDIPS), makes use of an iterative finite-difference method to solve the Laplace equation for the magnetic field. While the spherical harmonics are global functions and their amplitudes depend on all of the magnetogram data, these data affect the solution only locally in the finite-difference approach, which leads to a solution that behaves better in the presence of large spatial gradients. As a result, the finite-difference method provides more accurate results at solar latitudes higher than those typically used in the spherical-harmonic-expansion methods (Tóth, van der Holst, and Huang, 2011).

The FDIPS model runs on a spherical grid that is uniform in longitude, sine of latitude, and radial direction. For the present work we ran the model with a resolution of 0.5° in longitude (720 longitudinal grid points), 9.3×10^{-3} in the sine of latitude (216 latitudinal grid points, which implies an effective latitude resolution of 0.5° to 1.0° in the $\approx \pm 65^\circ$ latitude range), and $5 \times 10^{-3} R_\odot$ in the radial direction. Note that the dimension in each angular direction was chosen to be an integer fraction of the respective dimension in the MDI magnetogram. In this way, the cells of the magnetogram can be merged without losing magnetic flux.

The coronal magnetic field is globally well described by PFSS models, except in coronal regions where high currents are present, such as could be the case around filaments. However, for the purposes of our work, a PFSS model describes the connectivity of the magnetic field around the isolated and stable AR 10978 reasonably well. This is illustrated in Figure 3, which shows the result of our PFSS model when AR 10978 was at the central meridian. The displayed field lines were traced from a set of coronal starting points separated by 10° (in both latitude and longitude) and are located at a height of ≈ 50 Mm above the photosphere. This selection provides a fairly uniform sampling of the large-scale structures, especially of the streamer arches above the AR. The magnetic-field line passing each selected starting point was then traced in both directions until the solar atmosphere base ($1.0 R_\odot$) or the source surface ($2.5 R_\odot$) is reached. The tracing was performed using a forward Euler method software package (www.lmsal.com/~derosa/pfsspack, `spherical_trace_field.pro`). Two points are noteworthy in Figure 3: First, a good agreement between the locations of the CHs and the AR loops is evident when comparing Figure 3 with Figure 2 and, second, AR 10978 is fully covered by the streamer-belt arcade (see also Figures 5a, 6a, and 6b in Culhane *et al.*, 2014). The latter suggests that it is very difficult for the plasma in EIS upflows, which cannot access open-field lines, to escape into the slow SW, despite the findings of Culhane *et al.* (2014).

3. Global Magnetic Field Topology of CR 2064

3.1. Coronal Magnetic Null-Points

Since the seminal works on the origin of flares (see, *e.g.*, Sweet, 1958), it has been thought that null points are the topological structures in the solar corona in which magnetic-field reconnection and energy release is most likely to occur. In view of the results of van Driel-Gesztelyi *et al.* (2012), who found that magnetic-field lines in the vicinity of a null point can undergo interchange reconnection and channel AR plasma into the slow SW, we searched for null points in CR 2064.

The field connectivity in the neighbourhood of a null point displays a structure that is characterised by the so-called spines and fans (see, *e.g.*, Longcope, 2005; Pontin, 2011). Several works have analysed, either numerically (Craig and Fabling, 1996, 1999; Wyper and Pontin, 2013) or analytically (Ji and Song, 2001; Wilmot-Smith and Hornig, 2011), solutions for fan and spine magnetic reconnection. Observationally, the origin of several flares can be attributed to magnetic reconnection in the fan or spine structure of null points (*e.g.* Mandrini *et al.*, 1991, 1993, 2006, 2014; Parnell, Priest, and Golub, 1994; Aulanier *et al.*, 2000; Manoharan and Kundu, 2005; Luoni *et al.*, 2007; Reid *et al.*, 2012); although others are not related at all to their presence (*e.g.* Démoulin, Hénoux, and Mandrini, 1994; Mandrini *et al.*, 1996; Bagalá *et al.*, 2000; Schmieder *et al.*, 2007; Savcheva, van Ballegooijen, and DeLuca, 2012).

From a mathematical point of view, the neighbourhood of a magnetic null point can be described by the linear term in the local Taylor expansion of the magnetic field (see Démoulin, Hénoux, and Mandrini, 1994, and references therein). Diagonalisation of the Jacobian field-matrix gives three eigenvectors and the corresponding eigenvalues, which add up to zero to locally satisfy the divergence-free condition on the field. Under coronal conditions, the eigenvalues are real (Lau and Finn, 1990). A positive null point has two positive fan eigenvalues and conversely for a negative null. When a null point is present, the coronal volume is divided into two connectivity domains, which are separated by the surface of the fan. In each of these domains a spine is present. We refer to the lower (upper) spine as the one arising from below (above) the fan surface. This surface is defined by all of the field lines that start at an infinitesimal distance from the null in the plane defined by the two eigenvectors associated with the eigenvalues that have the same sign.

The method to locate the magnetic null-points in CR 2064 is similar to that discussed by Démoulin, Hénoux, and Mandrini (1994), but uses a spherical geometry for the coronal-field model. For a large sub-area of the whole photospheric map shown in Figure 1, Figure 4 shows the location of all of the null points found at a height of 25 Mm or greater above the photosphere within the displayed range. The threshold height of 25 Mm has been arbitrarily chosen for the figure. We carried out several searches for nulls using different threshold heights and found that their number decreases rapidly with height above the photosphere, as was shown by Longcope and Parnell (2009) for PFSS models constrained by quiet-Sun MDI magnetograms, and Schrijver and Title (2002) using a modelled boundary condition consisting of a random distribution of magnetic sources. Furthermore, for any threshold height $\lesssim 25$ Mm most of the null points found are not related to either AR 10978 or to the EIS upflows at its edges, or they present a closed-magnetic field structure (as we show in Section 3.2 for some of the nulls in Figure 4). These characteristics do not make these nulls good candidates for magnetic reconnection that enables the plasma of EIS upflows to reach the SW; therefore, they can be ignored.

Following Démoulin, Hénoux, and Mandrini (1994) (see also Mandrini *et al.* 2006, 2014), Figure 4 shows the location of all null points within an angular distance of 20° in

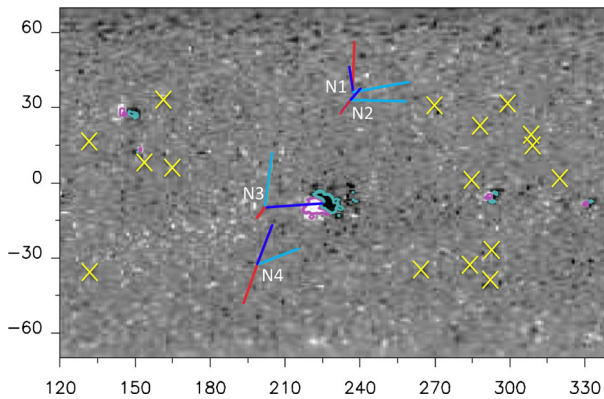


Figure 4 A section of the synoptic map of CR 2064. The magnetic field, which corresponds to the photospheric boundary of the PFSS model, is saturated above (below) 30 G (-30 G). The locations of all magnetic null-points at heights greater than $0.036 R_{\odot}$ (≈ 25 Mm) above the photosphere are shown either as the intersection of a set of three coloured segments (see text) when they are within 20° in longitude from AR 10978, or with a yellow \times -symbol when they are further away in longitude. Nulls identified by the three segments are also labelled with a letter and a number. The horizontal (vertical) axis is the Carrington longitude (latitude).

longitude from AR 10978 as the intersection of a set of three coloured segments, which correspond to the direction of the three eigenvectors of the Jacobian matrix. The colours of these segments indicate the magnitude of the corresponding eigenvalue: Red (yellow) corresponds to the highest (lowest) positive eigenvalue in the fan plane, blue to the spine eigenvalue for a positive null point. For a negative null, dark blue (light blue) corresponds to the highest (lowest) negative eigenvalue in the fan plane, red to the spine eigenvalue. These null points are also labelled with a letter and a number, and their magnetic structure is analysed in detail in Sections 3.2 and 3.3. The locations of nulls farther away than 20° in longitude from AR 10978 are indicated with a yellow \times -symbol.

To test the stability of the nulls identified in Figure 4, we computed their locations, eigenvectors, and eigenvalues using two alternative PFSS models: i) doubling the resolution of the previous model, and ii) keeping the same resolution, but changing the boundary condition to a synoptic map of CR 2064 from the *Global Oscillation Network Group* (GONG). GONG maps have a lower resolution, about ten times coarser than that of MDI, with 360 data points linear in longitude (or a resolution of 1°) and 180 data points linear in sine of latitude (against the 1080 data points of MDI). In performing experiment i), we found that the change in resolution kept the location of the nulls unaltered within a precision of $\approx 10^{-3}$ and preserved the characteristics of their topology (signs and relative values of the eigenvalues). In performing experiment ii), we found a similar result, with the location of the nulls being unaltered in radius and latitude within a precision of $\approx 10^{-2}$, and in longitude within a precision of $\approx 10^{-1}$. From these results, we conclude that the null points are indeed stable, and their presence and characteristics are not an artefact of the particular data set used as the boundary condition for the model and/or its numerical resolution.

3.2. Nulls with Closed Magnetic Configuration in the Neighbourhood of AR 10978

In Figures 5, 6, and 7, we show selected field lines that pass through locations in the vicinity of each null, N1 to N4. At each null, the eigenvectors that correspond to the spine line and the fan plane were computed. This information was used to select a number of position vectors around each null point, to be used as starting points to trace field lines.

Figure 5 Magnetic nulls with a large-scale and closed magnetic configuration around AR 10978. (a) Nulls 2, 3, and 4 and a set of field lines computed from their surroundings, as explained in Sections 3.1 and 3.2. The field lines drawn around N3 are connected to the network close to AR 10978, while those around N4 reach its western negative polarity. All field lines (drawn in black) computed for this set of nulls are closed. (b) A close-up and rotated view of null N4 illustrating a set of fan field lines and the upper spine line drawn in black and in red.

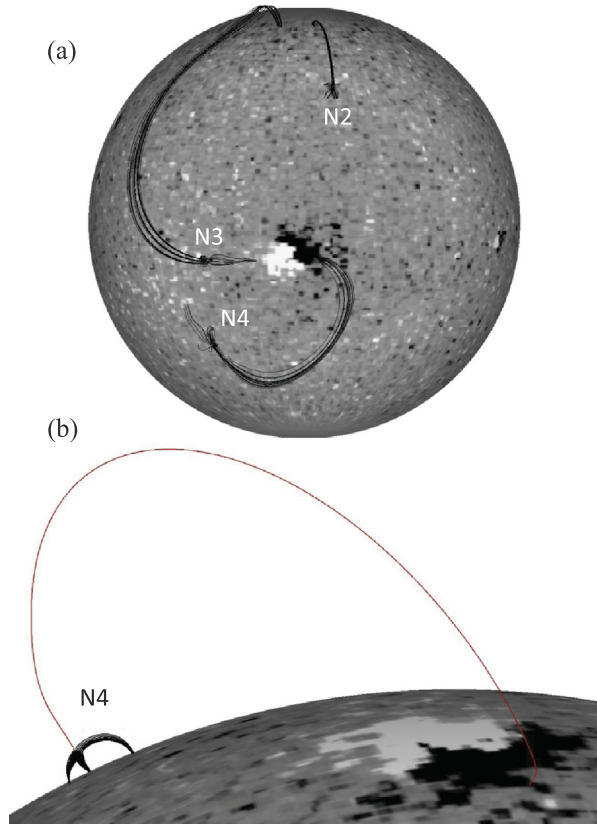


Figure 5a shows the magnetic connectivity in the vicinity of nulls N2, N3, and N4, which are all negative null points, located above the photosphere at heights 25.2, 26.4, and 25.7 Mm, respectively. To trace field lines for this figure we selected several starting points around each null, above and below their fan planes. The selected field lines clearly show that their large-scale magnetic configuration is closed. The upper spine of null N2 connects far away, towards the northern CH. Field lines around the upper spine of null N4 connect to the western negative polarity of AR 10978, while some field lines around N3 reach the network close to its eastern positive polarity at one footpoint and the northern CH at the other footpoint.

Figure 5b shows, as an example, a set of the fan field lines of null N4. To trace field lines, we selected several starting points in the fan plane, which were computed as the null position plus linear combinations of the two fan eigenvectors. We also selected a starting point along the spine line, computed as the null position plus an infinitesimal departure along the spine eigenvector. The field lines chosen to start in the fan plane are shown in black, while the upper spine line is shown in red.

3.3. Nulls with Open Magnetic Configuration in the Neighbourhood of AR 10978

The only magnetic null point associated with an open magnetic-field configuration is null N1 (Figure 6). It is located north-west of the main negative polarity of AR 10978, close to the northern negative CH. Its height above the photosphere is ≈ 108 Mm. The starting points

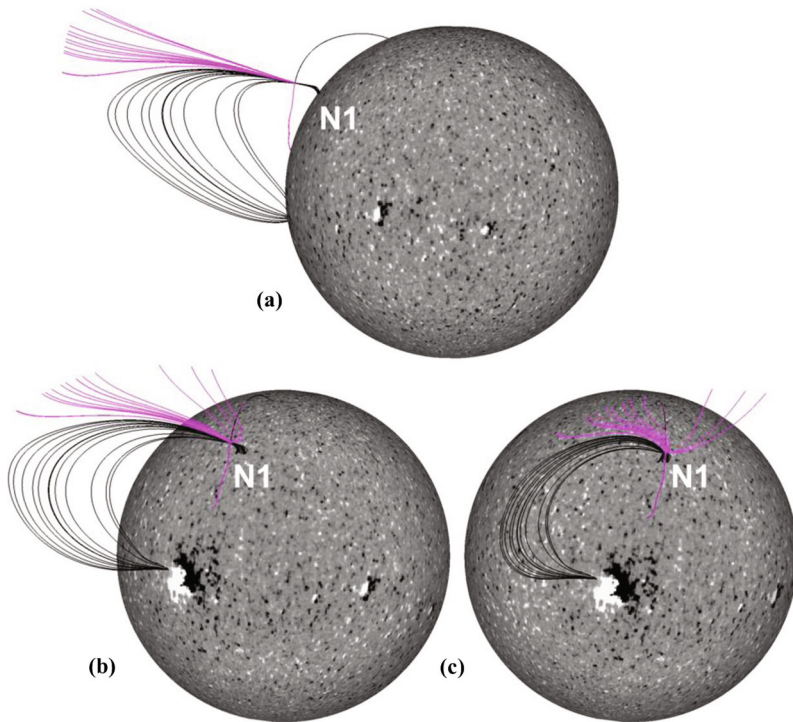
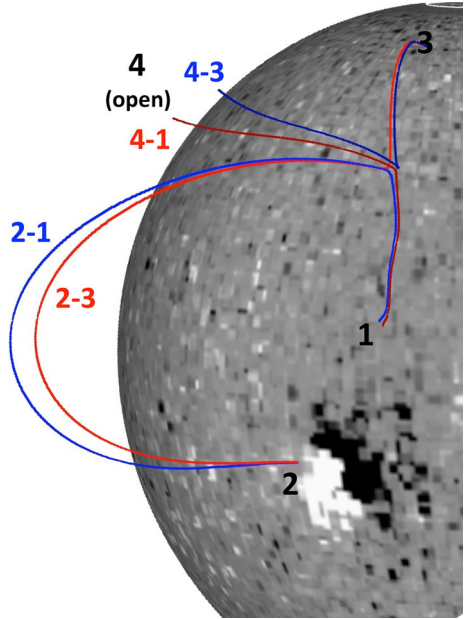


Figure 6 Different views of a set of field lines that pass in the neighbourhood of null point N1. The panels are different views of the same model. From the set of null points selected within $\pm 20^\circ$ in longitude from AR 10978, null N1 is the only one associated with an open magnetic-field configuration. (a) Corresponds to what an observer facing the Sun would see when the centre of AR 10978 was at the eastern limb. (b) and (c) correspond to what the same observer would see when the centre of the AR was at solar longitudes of 45° and 0° . Open-field lines anchored in negative-polarity field are drawn in pink, while closed-field lines are drawn in black. Note that in (a) the open-field lines, rooted in the negative polarity, shift towards the Ecliptic at the source surface as their photospheric footpoints shift slightly towards the solar Equator (compare panels a to b).

for tracing the field lines around this null were selected on a $3 \times 7 \times 7$ (radial \times latitudinal \times longitudinal) spherical grid centred on its location, with a $0.02 R_\odot$ grid step in the radial direction and a 0.5° step in both angular directions. Only a subset of 49 points with heights greater than that of the null are chosen for the field lines drawn in Figure 6, where they are shown from three different points of view. Figure 6a shows that the open-field lines around the upper spine slightly shift towards the Ecliptic at the source surface as their footpoints lie closer to the solar Equator (compare panel a and b). The other two points of view correspond to an intermediate one (panel b) and to the AR seen at its CMP (panel c).

Figure 7 shows a selection of four field lines from the set in Figure 6 in the neighbourhood of null N1. These selected field lines illustrate how reconnection could proceed at this null. Large-scale loops anchored close to the following polarity of AR 10978, labelled 2–1, could reconnect with open-field lines from the northern CH, labelled 4–3, to give (*via* interchange reconnection) field lines labelled 2–3 and 4–1. This process would transfer the closed-loop coronal plasma to the open field and displace the footpoints of the open-field lines towards the solar Equator. As a consequence, at the source surface these reconnected open-field lines would shift towards the Ecliptic. However, this one-step reconnection process

Figure 7 A selection of four field lines computed from the vicinity of null point N1. These have been chosen from the set in Figure 6 to illustrate how interchange reconnection could proceed at the null. Even (odd) numbers at the photospheric level indicate positive (negative) polarity regions to which the field lines are connected. Number 4 is used for the source surface at $2.5 R_{\odot}$. Numbers separated with a dash, set by each field line, indicate its connectivity. The field lines have been coloured such that blue corresponds to pre-reconnection closed and open-field lines, while red corresponds to post-reconnection closed and open-field lines.



is not sufficient to bring the plasma contained in the AR upflows into the open field (see Section 3.4).

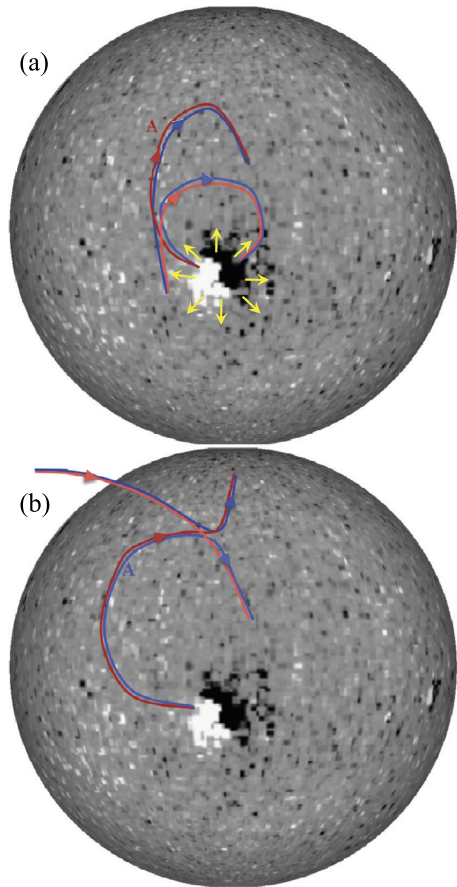
3.4. How Can the AR Plasma Escape into the SW?

As discussed in Section 2 and illustrated in Figures 2 and 3, AR 10978 lies completely below the streamer belt. This means that even if some field lines anchored close to its following positive polarity could reconnect with the northern CH open lines at null N1 (see Section 3.3), this interchange reconnection process cannot bring the plasma in the closed loops at the periphery of the AR directly into the SW.

The combination of the magnetic topology analysis we discussed in Section 3.3 with the results of Baker *et al.* (2009) for a different AR provides a way for the plasma in EIS upflows to reach the SW. In a first step, the AR expansion could force reconnection at QSLs between the AR closed loops at its borders and large-scale network fields anchored east of the region; these pre-reconnected field lines are drawn in blue in the sketch of Figure 8a. As a result of this process, the reconnected field lines, drawn in red, will connect the positive network field east of the AR to its preceding negative polarity and to the network north of the region. In this way, the plasma in the EIS upflows, mainly from the eastern side of the AR and to a lesser degree from the western side, could gain access to field lines similar to those labelled A (see Figure 8a). These field lines represent pre-reconnection field lines in a second reconnection process.

In a second step, illustrated in the sketch of Figure 8b, the subsequent diffusion of the photospheric AR field could induce the reconnection of the previous large-scale field lines, in particular field lines similar to A (compare the two panels in Figure 8), with the open ones anchored in the neighbourhood of the northern negative CH. This reconnection process may occur at null N1, located north-west of the AR, and associated separatrices, as we have discussed in Section 3.3. As reconnection proceeds, the reconnected open-field lines would

Figure 8 Sketch showing how the AR plasma can be injected into the solar wind after a minimum of two main reconnection steps. In blue continuous lines we depict the field lines before reconnection, while in red and pink we show the post-reconnection field lines. (a) The AR expansion, indicated by yellow arrows, forces reconnection between the AR closed loops and the network large-scale field lines. (b) The further diffusion of the photospheric AR field induces reconnection with the open field of the northern CH. As a result, plasma of AR origin injected in the large-scale closed loops by the first reconnection, can reach the solar wind. The reconnected open-field lines progressively bend towards the Ecliptic (see Figure 6) and the AR plasma can be later detected at 1 AU by the ACE spacecraft.



bend progressively towards the Ecliptic (see Figure 6) so that plasma of AR origin could later be detected at 1 AU. We speculate that the two-step reconnection scenario, based on the finding of a null point associated with field lines that are open towards the interplanetary space in our PFSS model, is the only way through which plasma contained in originally closed AR 10978 field lines can be released into the SW. In practice, more reconnection steps are likely, mainly within QSLs where a continuous slipping reconnection process has been found to be at work (Aulanier *et al.*, 2006).

4. Evidence of the Two-Step Magnetic Reconnection Process

4.1. Characteristics of the Radio Emission

The reconnection processes described above occur in regions where the magnetic-field intensity is low; hence, we do not expect to find evidence of the energy released in wavelength ranges such as the EUV or the visible. We therefore analysed the radio emission at frequencies sensitive to weak energy release. Excluding more eruptive transient phenomena, noise storms at metric and decimetric wavelengths are the oldest evidence of electron acceleration in the solar corona. Radio emission of a noise storm consists of a broad-band continuum

lasting from a few tens of minutes to a few days with superimposed Type I bursts of short duration and of narrow spectral bandwidth (typically a few MHz). They are mainly observed in the 100–500 MHz frequency range. The consensus is that noise-storm emission is triggered by supra-thermal electrons (few keVs), which produce Langmuir waves that are subsequently converted into electromagnetic radiation near the local plasma frequency. This explains the strong polarisation observed in the ordinary mode and also the high value of the brightness temperature (see for example Kundu, 1965; Melrose, 1980; Wentzel, 1986). Le Squeren (1963) determined that the emission at 169 MHz during noise storms comes from layers located between 60 and 600 Mm (0.09–0.85 R_{\odot}) above the photosphere and, in general, from much higher altitudes than those estimated for an unperturbed normal corona. At the same frequency, Kerdraon and Mercier (1982) found a mean altitude of 130 Mm (0.16 R_{\odot}) for a series of selected noise storms they analysed. Interestingly, centres of noise storms are not situated radially above sunspot groups.

The *Nançay Radioheliograph* (NRH; Kerdraon and Delouis, 1997), with an operational frequency range between 150 and 432 MHz, allows imaging of weak energy release at coronal heights such as those where noise storms originate. Considering Coulomb collisions with ambient electrons as the energy-loss mechanism, Raulin and Klein (1994) showed that electrons with energies required to produce noise storms have lifetimes of tens of seconds for ambient densities between $3 \times 10^8 \text{ cm}^{-3}$ and $2 \times 10^9 \text{ cm}^{-3}$, which correspond to the plasma frequencies in the NRH operational range. These densities are typical of the low and middle corona (≈ 0.1 – $0.5 R_{\odot}$ above the photosphere).

Ionospheric effects scale as ν^{-2} (Bougeret, 1973) and are mainly due to electron-density fluctuations caused by atmospheric gravity waves, which produce travelling ionospheric disturbances (TIDs). At metric wavelengths the only effect of TIDs is a periodic shift of the radio source location (Mercier, Genova, and Aubier, 1989), which is evident in radio observations made in general before noon (Spoelstra and Kelder, 1984; Mercier, 1986a, 1986b).

4.2. NHR Observations on 13 December 2007

We examined NRH radio observations from 8 to 13 December 2007 for their complete observing time. Throughout this period, we found slightly enhanced emission over AR 10978 that lasted a few hours and, occasionally, other sources at different locations on the disc. On 13 December, the enhancements over AR 10978 were continuously present during the full NRH observing period (9:00–15:00 UT). These enhancements can be considered as the signatures of noise storms. We interpret the enhanced emission over the AR as being caused by electrons accelerated by reconnection at the QSLs shown in Figure 7 of Démoulin *et al.* (2013). These accelerated electrons travel along the closed (reconnected) loops anchored at both of the AR borders. Consistent with this interpretation, the intensity isocontour, at 80 % of its maximum, in the highest NRH frequency clearly encloses AR 10978 (this has been added in blue continuous line to Figure 10). A similar origin can be attributed to the 150.9 MHz isocontour (added as a red continuous line to the same figure). Taking into account the projection effect, this lowest-frequency contour is well aligned with the top of a loop arcade south-west of the AR, which is anchored at both of its borders.

We are not interested here in the radio emission located directly over AR 10978, however, but in its vicinity, because we seek evidence of the two-step reconnection process proposed to explain how the AR plasma can gain access to the SW (Section 3.4). Furthermore, as a by-product of our topological analysis, we also found null points that were not linked to EIS upflows (Section 3.2). We also investigate whether magnetic reconnection at these external nulls might be the cause of the sporadic bursts. Therefore, we searched for sources of sporadic emission at 150.9 MHz, which is the lowest NRH frequency and the one which most

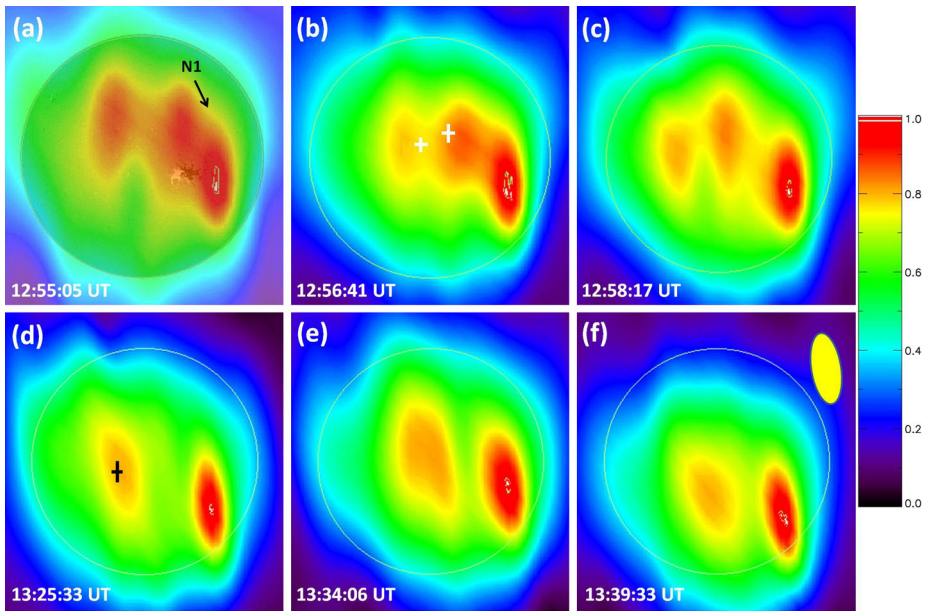


Figure 9 (a), (b), and (c): Brightness distribution over the solar disc at 150.9 MHz in the period 12:55–13:00 UT on 13 December 2007. In addition to the main emission associated with the AR (west-ernmost feature in each image), we observe different locations of dynamically varying radio-emission that eventually reach levels similar to those of the noise storm above the AR. The white crosses in (b) indicate the average position of the two main fluctuating sources and the uncertainty of their locations is given by the size of the crosses. The image (partially transparent) in panel a has been superimposed on the MDI full-disc magnetogram on 13 December 2007 at 12:45 UT. The arrow points to the location of null N1. (d), (e), and (f): Similar to the top panels, but for the 13:25–13:40 UT period. The average position of the sources is now indicated by a black cross and its size is a measure of their location uncertainty. The yellow ellipse in panel f indicates the beam size and its orientation computed at 13:00 UT. This lobe is computed at half the maximum beam power, and its size implies that the observed sources are not resolved. The brightness distribution of each image has been normalised to its highest value, and the bar to the right indicates the colour scale.

likely shows signatures of Type I bursts. We analysed the brightness distribution over the solar disc on 13 December with a temporal cadence of one second, choosing the time interval for which the ionospheric effects would be weakest (12:30–13:40 UT). We verified that this was the case by examining the east–west and north–south one-dimensional brightness distribution diagrams (www.secchirh.obspm.fr/index.php) at 150 and 432 MHz for this day. In addition to the enhanced emission over the AR, we observed regions where the emission fluctuates and recurrently increases and decreases, as shown in Figure 9. To determine the appearance of these sporadic sources in a more systematic way, we used the specific software developed for NRH data analysis that is included in the Solar Soft package. We scanned NRH images at 150.9 MHz during limited periods of time, no longer than 15 minutes, using a square window not larger than $0.25 R_{\odot}$. Proceeding in this way, we found sources between 12:55 and 13:10 UT and between 13:25 and 13:40 UT. Panels a–c in Figure 9 illustrate the brightness distribution at three different hours during the first time interval, while panels d–f correspond to the second one. The sources are not static because they appear at a slightly different location in each image. The white crosses in Figure 9b indicate the average locations of the highest intensity of the two main sporadic sources found in the first time interval (12:55–13:10 UT). The size of the cross arms indicates the statistical dispersion (1σ) in

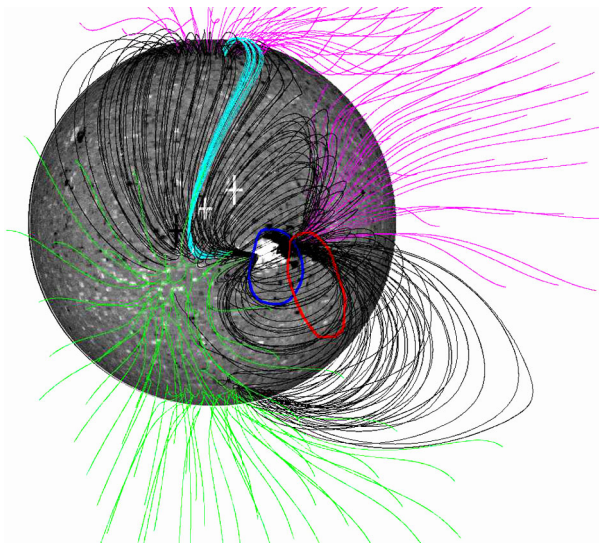


Figure 10 Magnetic-field lines calculated from the PFSS model rotated to the same time as that of NRH emission isocontours (13:25 UT on 13 December). To the randomly computed field lines starting integration at 50 Mm above the photosphere, we have added a set of lines in the neighbourhood of null point N3, drawn in light blue. The convention for the field line colour, except for those associated with null N3, is the same as in Figure 3. The magnetic field has been saturated above (below) 300 G (-300 G). Superimposed we show isocontours of NRH radio emission at 432 (blue) and 150.9 (red) MHz. Their intensity corresponds to 80 % of the maximum and they have been obtained with approximately one-minute integration. At the highest frequency, the emission is concentrated over the AR and encloses it, while the 150.9 MHz contour appears to be shifted south-west of the AR (see Figure 9). We have also added the white and black crosses shown in Figure 9b and d, which are at the average locations of the sporadic sources during the two time intervals studied in detail (see Section 4.2).

the position estimate. The black cross in Figure 9d illustrates a similar result for the second time interval (13:25–13:40 UT). We have chosen to represent the variable position of the sporadic sources by their averaged location in each time interval (white and black crosses in Figure 9) because we consider it to be the most convenient way for comparison with a global and static coronal-field model (see next paragraph).

Furthermore, to ensure that the observed sporadic sources are not of ionospheric origin, we plotted their intensity *vs.* time (not shown) and compared these intensity curves with the standard deviation of the continuum corresponding to each of the two time intervals. The standard deviations were taken as an upper limit of the ionospheric influence; their values were at least an order of magnitude lower than the typical intensity of any of the sporadic-source curves. Therefore, we conclude that the observed bursty sources have a true solar origin.

4.3. Signatures of the Two-Step Reconnection Process

To understand the origin of the sporadic emission in 150.9 MHz during the two time intervals discussed in the previous paragraphs, we compared their average locations (white and black crosses in Figure 9) with field lines computed using the PFSS model described in Section 3. This is illustrated in Figure 10. Comparing this figure with Figure 9, it is clear that the bursty-emission sources are associated with closed magnetic-field lines. Indeed, a visual

comparison of Figures 9 and 10 reveals that the location of the sporadic sources is distributed along and within the arcade of the large-scale closed loops that shape the streamer belt. These bursts may originate from magnetic reconnection between field lines anchored at the periphery of AR 10978 and closed-field lines with one end connected to the quiet-Sun east of the AR and the other one anchored far north of it. In this case, reconnection is presumably forced by the magnetic-field dispersion of AR 10978 at successively different locations. That is why we observe several sources and their locations vary in a dynamic way. Therefore, we conclude that these sporadic sources can be considered as the coronal manifestation of the first step in the proposed reconnection process (Figure 8a). Figure 10 also includes a set of field lines computed in the neighbourhood of null point N3 (see Figure 5), which were selected with a higher spatial density and are highlighted in light-blue. The spatial closeness between this set of field lines and the black and white crosses suggests that, eventually, some of the observed sporadic sources could be the signature of energetic electrons accelerated by magnetic reconnection at null point N3. The location where the emission is observed will, in particular, depend on the ambient-plasma density. Furthermore, if the energy released in the process were not high enough, the emission might not be detectable all along the reconnected loops.

Finally, our previous analysis indicates that at the lowest NRH frequency we observe no radio signature of the second step in the reconnection process sketched in Figure 8b. The noise storms we found in the vicinity of AR 10978 are related to closed-loop configurations, as was shown in several other examples (Stewart, 1977; Svestka, 1983; Gnezdilov and Fomichev, 1987; Lang, Trotter, and Willson, 1988; Böhme, 1989; Krucker *et al.*, 1995; Iwai *et al.*, 2012). This contrasts somewhat with the suggestion by Del Zanna *et al.* (2011), who observed a low-frequency Type III noise-storm jointly with a metric noise-storm and associated both emissions to open-field line configurations. We also searched for evidence of Type III bursts, which are known to be caused by electrons that are accelerated outwards along the open coronal-field lines (see for example Suzuki and Dulk, 1985; Bastian, Benz, and Gary, 1998; Pick and Vilmer, 2008). Type III bursts were observed neither by the *Nançay Decameter Array* (20–70 MHz) nor by the *Waves* experiment (40 kHz–14 MHz) onboard the *Wind* spacecraft. This means that we found no evidence of electron acceleration originating at null N1 in the open coronal field. However, we have to take into account the fact that despite the wide dynamic range of the *Nançay Decameter Array* (wider than 60 dB, Lecacheux, 2000), a strong source such as an active region can prevent the detection of weak Type III bursts.

5. Summary and Implications for the Slow Solar Wind

After the launch of *Hinode*, upflows that lasted for several days were observed at the borders of ARs, both with XRT and EIT. These observations posed questions about the possible contribution of the upflowing plasma to the slow SW. Several works considered the problem using different approaches, either by computing the magnetic-field topology to explain their origin and how they might reach the SW, or by comparing their composition with that of the slow SW (see references in Section 1). The link was found by van Driel-Gesztelyi *et al.* (2012) through a combined analysis of coronal and *in-situ* observations, together with local and global magnetic-field modelling and topology computation. These authors analysed EIS observations of a region that crossed the solar disc during CR 2065. During this rotation, AR 10980, the recurrence of AR 10978 that we studied here, and a small spotless bipolar region formed a quadrupolar large-scale topology. It was proposed that magnetic reconnection at

a high-altitude null point, found in the configuration, directed part of the upflowing plasma into the slow SW. During CR 2064, AR 10978, where prominent EIS upflows are observed, is an isolated, simple bipolar region that is completely enclosed by the large-scale loops of the streamer belt (see Section 2). In passing over the AR, the projection of the HCS, determined from a GONG PFSS model, roughly aligns with the AR main polarity inversion line, leaving its negative polarity to its western side.

We performed a detailed topological analysis of the region and its surroundings to determine how the plasma in the EIS upflows at both sides of AR 10978 might have been injected into the SW. From our computations, based on a PFSS model, we identified four high-altitude magnetic null-points (Section 3.1) located at heights of 25 Mm or higher above the photosphere and within 20° in longitude from the region. The AR polarities are directly linked to only two of these null points (labelled N3 and N4 in Figures 4 and 5). These two null points are associated with closed-field configurations. A third null point (labelled N2 in Figures 4 and 5) is located far north and is not directly connected to the AR. This null point also presents a closed-field configuration. Therefore, magnetic reconnection at these nulls cannot provide a path for the upflowing plasma into the slow SW (Section 3.2).

The fourth null point (labelled N1 in Figures 4 and 6), located north-west of AR 10978 and at a height of ≈ 108 Mm, is the only one linked to open-field lines. A magnetic-interchange reconnection process could occur at this null point (as illustrated in Figure 7) and, in this way, the coronal plasma could be channelled into the SW. However, field lines computed from this null-point neighbourhood are not directly connected to AR 10978. This means that to bring the plasma in EIS upflows into the open coronal field, we need a reconnection process that works in more than one step. In a first step, the AR expansion forces reconnection at QSLs between the AR closed loops at its borders and large-scale network fields anchored east of the region. As a result of this process, which is illustrated in Figure 8a, plasma in the EIS upflows, mainly from the eastern side of the AR but also from the western side, is injected into large-scale loops that are anchored close to the following polarity of AR 10978. In a second step, these large-scale loops can undergo interchange reconnection with open-field lines from the northern CH, as shown in Figures 7 and 8b. The reconnected open-field lines that result from this process are anchored to the negative network field on the Sun's surface at one end and reach the source surface at the other end. The two-step process brings the upflowing plasma into the open field and, at the same time, displaces the solar connectivity of the open field towards the solar Equator and, thus, towards the Ecliptic at the source surface.

The results from our topological analysis imply that plasma with a typical AR composition should be found in the negative SW sector in front of the HCS at 1 AU. This is, indeed, what Culhane *et al.* (2014) found from studying *in-situ* ACE observations at 1 AU. Using a back-mapping technique and analysing three characteristics of the SW plasma that was measured before the HCS crossing, these authors were able to associate the origin of the SW plasma with AR 10978. Firstly, the C^{6+}/C^{5+} and O^{7+}/O^{6+} ratios were found to be enhanced, which is a signature of a higher frozen-in temperature origin in the corona. Secondly, they determined that in the time period when AR 10978 was crossing the CM, the FIP-bias for the eastern upflow was in the range 3.5 to 4.0 (characteristic of closed AR structures), while the Fe/O ratio measured by ACE also increased by a factor of three to four just before the HCS crossing. Finally, it was found that in the same period the He density was depleted compared with the proton density, which is consistent with the passage of ACE across the streamer belt. Therefore, the slow-SW plasma observed by ACE before the HCS crossing seems to have a significant contribution from AR 10978 upflowing plasma. Furthermore, these authors showed that ACE detection of the previously described plasma

characteristics began five days after AR 10978 reached CM. The time interval for this detection, considering typical slow-SW velocity values, should be around three days; in view of this time difference, Culhane *et al.* (2014) concluded that the longer elapsed time could be explained by the addition of the plasma travel time from AR 10978 to null N1, which supports the two-step reconnection process described in the previous paragraph.

The reconnection processes discussed above occur in regions where the magnetic-field intensity is low. Therefore, to find coronal signatures of the energy released, we analysed the radio emission from NRH at frequencies in the range 150–432 MHz. We found a set of sporadic sources located along and within the large-scale arcade of closed loops that form the streamer belt. These dynamically varying sources are identified during two different time intervals. Their locations (Figures 9 and 10) and evolution suggest that they may originate from magnetic reconnection between field lines anchored at the borders of AR 10978 and closed-field lines with footpoints in quiet-Sun regions east of the AR and far to its north. This reconnection process is presumably forced by the magnetic-field dispersion of AR 10978 at successively different locations. We interpreted the presence of these sporadic sources as the coronal manifestation of the first step of the proposed reconnection process (Figure 8a) with, eventually, a contribution to energy release at null point N3. However, we found no radio-emission evidence of the second reconnection step process that should occur at null N1. This second step is supported by the presence of plasma with AR composition in the SW at 1 AU.

For the particular case of AR 10978, our results show how plasma from the eastern and western EIS upflows was observed *in-situ* by ACE. This requires an indirect process that involves magnetic reconnection in at least two steps. Our analysis extends that of van Driel-Gesztelyi *et al.* (2012), who showed that part of the AR upflows could become outflows *via* direct interchange magnetic reconnection at a high-altitude magnetic null point. Our results, based on observational evidence and the topological properties of the magnetic-field configuration, demonstrate that even when it appears highly improbable for the AR plasma to reach the SW, indirect channels involving a sequence of reconnections at QSLs and high-altitude null points may make it possible. Furthermore, to understand the full process, studies such as the one presented here need to be complemented by a detailed analysis of several parameters observed *in-situ* (*i.e.* plasma velocity, density, composition, and magnetic field) together with the determination of the outflowing-plasma composition.

Acknowledgements We thank the anonymous referee, whose comments improved this article. We also thank A. Kerdran for his help in processing NRH data. CHM and GDC acknowledge financial support from the Argentinean grants PICT 2007-1790 (ANPCyT), UBACyT 20020100100733, and PIP 2009-100766 (CONICET). The research leading to these results has received funding from the European Commission's Seventh Framework Programme under the grant agreement No. 284461 (eHEROES project). LvDG and DB acknowledge support by STFC Consolidated Grant ST/H00260/1. LvDG's work was supported by the Hungarian Research grant OTKA K-081421. CHM, AMV, and GDC are members of the Carrera del Investigador Científico (CONICET). FAN is a fellow of CONICET. We thank D.M. Long for the enhanced XRT image and H. Morgan for the XRT processing software.

References

- Antiochos, S.K., DeVore, C.R., Karpen, J.T., Mikić, Z.: 2007, *Astrophys. J.* **671**, 936. DOI. ADS.
- Antiochos, S.K., Mikić, Z., Titov, V.S., Lionello, R., Linker, J.A.: 2011, *Astrophys. J.* **731**, 112. DOI. ADS.
- Antiochos, S.K., Linker, J.A., Lionello, R., Mikić, Z., Titov, V., Zurbuchen, T.H.: 2012, *Space Sci. Rev.* **172**, 169. DOI. ADS.
- Aulanier, G., DeLuca, E.E., Antiochos, S.K., McMullen, R.A., Golub, L.: 2000, *Astrophys. J.* **540**, 1126. DOI. ADS.

- Aulanier, G., Pariat, E., Démoulin, P., Devore, C.R.: 2006, *Solar Phys.* **238**, 347. DOI.
- Bagalá, L.G., Mandrini, C.H., Rovira, M.G., Démoulin, P.: 2000, *Astron. Astrophys.* **363**, 779. ADS.
- Baker, D., van Driel-Gesztelyi, L., Mandrini, C.H., Démoulin, P., Murray, M.J.: 2009, *Astrophys. J.* **705**, 926. DOI.
- Bastian, T.S., Benz, A.O., Gary, D.E.: 1998, *Annu. Rev. Astron. Astrophys.* **36**, 131. DOI. ADS.
- Böhme, A.: 1989, *Solar Phys.* **122**, 13. DOI. ADS.
- Bougeret, J.L.: 1973, *Astron. Astrophys.* **24**, 53. ADS.
- Bradshaw, S.J., Aulanier, G., Del Zanna, G.: 2011, *Astrophys. J.* **743**, 66. DOI.
- Brooks, D.H., Warren, H.P.: 2011, *Astrophys. J. Lett.* **727**, L13. DOI. ADS.
- Brooks, D.H., Warren, H.P.: 2012, In: Bellot Rubio, L., Reale, F., Carlsson, M. (eds.) *4th Hinode Science Meeting: Unsolved Problems and Recent Insights CS-455*, Astron. Soc. Pac., San Francisco, 327. ADS.
- Bryans, P., Young, P.R., Doschek, G.A.: 2010, *Astrophys. J.* **715**, 1012. DOI.
- Craig, I.J.D., Fabling, R.B.: 1996, *Astrophys. J.* **462**, 969. DOI. ADS.
- Craig, I.J.D., Fabling, R.B., Heerikhuisen, J., Watson, P.G.: 1999, *Astrophys. J.* **523**, 838. DOI. ADS.
- Cranmer, S.R., van Ballegooyen, A.A., Edgar, R.J.: 2007, *Astrophys. J., Suppl. Ser.* **171**, 520. DOI. ADS.
- Culhane, J.L., Brooks, D.H., van Driel-Gesztelyi, L., Démoulin, P., Baker, D., DeRosa, M.L., Mandrini, C.H., Zhao, L., Zurbuchen, T.H.: 2014, *Solar Phys.* **289**, 3799. DOI. ADS.
- Del Zanna, G., Aulanier, G., Klein, K.-L., Török, T.: 2011, *Astron. Astrophys.* **526**, A137. DOI.
- Démoulin, P., Hénoux, J.C., Mandrini, C.H.: 1994, *Astron. Astrophys.* **285**, 1023. ADS.
- Démoulin, P., Hénoux, J.C., Priest, E.R., Mandrini, C.H.: 1996, *Astron. Astrophys.* **308**, 643. ADS.
- Démoulin, P., Baker, D., Mandrini, C.H., van Driel-Gesztelyi, L.: 2013, *Solar Phys.* **283**, 341. DOI. ADS.
- Feldman, U., Widing, K.G.: 2003, *Space Sci. Rev.* **107**, 665. DOI. ADS.
- Fisk, L.A.: 2003, *J. Geophys. Res. (Space Phys.)* **108**, 1157. DOI. ADS.
- Fisk, L.A., Schwadron, N.A., Zurbuchen, T.H.: 1998, *Space Sci. Rev.* **86**, 51. DOI. ADS.
- Fisk, L.A., Zhao, L.: 2009, In: Gopalswamy, N., Webb, D.F. (eds.) *Universal Heliophysical Processes, IAU Symposium 257*, Cambridge University Press, Cambridge, 109. DOI. ADS.
- Foullon, C., Lavraud, B., Luhmann, J.G., Farrugia, C.J., Retinò, A., Simunac, K.D.C., Wardle, N.C., Galvin, A.B., Kucharek, H., Owen, C.J., Popecki, M., Opitz, A., Sauvaud, J.-A.: 2011, *Astrophys. J.* **737**, 16. DOI. ADS.
- Gnezdilov, A.A., Fomichev, V.V.: 1987, *Pism'a Astron. ž.* **13**, 704. ADS.
- Gopalswamy, N., Mäkelä, P., Akiyama, S., Xie, H., Yashiro, S., Reinard, A.A.: 2013, *Solar Phys.* **284**, 17. DOI. ADS.
- Harra, L.K., Sakao, T., Mandrini, C.H., Hara, H., Imada, S., Young, P.R., van Driel-Gesztelyi, L., Baker, D.: 2008, *Astrophys. J. Lett.* **676**, L147. DOI.
- Holzer, T.E., Leer, E.: 1980, *J. Geophys. Res.* **85**, 4665. DOI. ADS.
- Iwai, K., Miyoshi, Y., Masuda, S., Shimojo, M., Shiota, D., Inoue, S., Tsuchiya, F., Morioka, A., Misawa, H.: 2012, *Astrophys. J.* **744**, 167. DOI. ADS.
- Ji, H.S., Song, M.T.: 2001, *Astrophys. J.* **556**, 1017. DOI. ADS.
- Kerdraon, A., Delouis, J.-M.: 1997, In: Trotter, G. (ed.) *Coronal Physics from Radio and Space Observations, Lecture Notes in Physics 483*, Springer, Berlin, 192. DOI. ADS.
- Kerdraon, A., Mercier, C.: 1982, In: Benz, A.O., Zlobec, P. (eds.) *Solar Radio Storms, CESRA Workshop #4*, Int. Rep. Os. Astron. Trieste, Trieste, 27. ADS.
- Krucker, S., Benz, A.O., Aschwanden, M.J., Bastian, T.S.: 1995, *Solar Phys.* **160**, 151. DOI. ADS.
- Kundu, M.R.: 1965, *Solar Radio Astronomy*, Interscience, New York. ADS.
- Lang, K.R., Trotter, G., Willson, R.F.: 1988, *Astron. Astrophys.* **199**, 325. ADS.
- Lau, Y.-T., Finn, J.M.: 1990, *Astrophys. J.* **350**, 672. DOI. ADS.
- Le Squeren, A.M.: 1963, *Ann. Astrophys.* **26**, 97. ADS.
- Lecacheux, A.: 2000, *Geophys. Monogr. Ser.* **119**, 321. ADS.
- Linker, J.A., Lionello, R., Mikić, Z., Titov, V.S., Antiochos, S.K.: 2011, *Astrophys. J.* **731**, 110. DOI. ADS.
- Longcope, D.W.: 2005, *Living Rev. Solar Phys.* **2**, 7. DOI. ADS.
- Longcope, D.W., Parnell, C.E.: 2009, *Solar Phys.* **254**, 51. DOI. ADS.
- Luoni, M.L., Mandrini, C.H., Cristiani, G.D., Démoulin, P.: 2007, *Adv. Space Res.* **39**, 1382. DOI. ADS.
- Mandrini, C.H., Demoulin, P., Henoux, J.C., Machado, M.E.: 1991, *Astron. Astrophys.* **250**, 541. ADS.
- Mandrini, C.H., Rovira, M.G., Demoulin, P., Henoux, J.C., Machado, M.E., Wilkinson, L.K.: 1993, *Astron. Astrophys.* **272**, 609. ADS.
- Mandrini, C.H., Démoulin, P., van Driel-Gesztelyi, L., Schmieder, B., Cauzzi, G., Hofmann, A.: 1996, *Solar Phys.* **168**, 115. DOI. ADS.
- Mandrini, C.H., Démoulin, P., Schmieder, B., Deluca, E.E., Pariat, E., Uddin, W.: 2006, *Solar Phys.* **238**, 293. DOI. ADS.
- Mandrini, C.H., Schmieder, B., Démoulin, P., Guo, Y., Cristiani, G.D.: 2014, *Solar Phys.* **289**, 2041. DOI. ADS.

- Manoharan, P.K., Kundu, M.R.: 2005, *Adv. Space Res.* **35**, 70. DOI. ADS.
- Masson, S., Pariat, E., Aulanier, G., Schrijver, C.J.: 2009, *Astrophys. J.* **700**, 559. DOI.
- McComas, D.J., Bame, S.J., Barraclough, B.L., Feldman, W.C., Funsten, H.O., Gosling, J.T., Riley, P., Skoug, R., Balogh, A., Forsyth, R., Goldstein, B.E., Neugebauer, M.: 1998, *Geophys. Res. Lett.* **25**, 1. DOI. ADS.
- Melrose, D.B.: 1980, *Solar Phys.* **67**, 357. DOI. ADS.
- Mercier, C.: 1986a, *Ann. Geophys.* **4**, 469. ADS.
- Mercier, C.: 1986b, *J. Atmos. Terr. Phys.* **48**, 605. ADS.
- Mercier, C., Genova, F., Aubier, M.G.: 1989, *Ann. Geophys.* **7**, 195. ADS.
- Miralles, M.P., Cranmer, S.R., Kohl, J.L.: 2004, *Adv. Space Res.* **33**, 696. DOI. ADS.
- Miralles, M.P., Cranmer, S.R., Panasyuk, A.V., Romoli, M., Kohl, J.L.: 2001, *Astrophys. J. Lett.* **549**, L257. DOI. ADS.
- Morgan, H., Jeska, L., Leonard, D.: 2013, *Astrophys. J., Suppl. Ser.* **206**, 19. DOI. ADS.
- Neugebauer, M., Liewer, P.C., Smith, E.J., Skoug, R.M., Zurbuchen, T.H.: 2002, *J. Geophys. Res. (Space Phys.)* **107**, 1488. DOI. ADS.
- Parker, E.N.: 1958, *Astrophys. J.* **128**, 664. DOI. ADS.
- Parker, E.N.: 1963, In: Daniel, R.R., Lavakare, P.J., Menon, M.G.K., Naranan, S., Nerurkar, N.W., Yash, Pal, Sreekantan, V.V. (eds.) *Inter. Cos. Ray Conf.* **1**, 175. ADS.
- Parnell, C.E., Priest, E.R., Golub, L.: 1994, *Solar Phys.* **151**, 57. DOI. ADS.
- Pick, M., Vilmer, N.: 2008, *Astron. Astrophys. Rev.* **16**, 1. DOI. ADS.
- Pontin, D.I.: 2011, *Adv. Space Res.* **47**, 1508. DOI. ADS.
- Raulin, J.P., Klein, K.-L.: 1994, *Astron. Astrophys.* **281**, 536. ADS.
- Reid, H.A.S., Vilmer, N., Aulanier, G., Pariat, E.: 2012, *Astron. Astrophys.* **547**, A52. DOI. ADS.
- Sakao, T., Kano, R., Narukage, N., Kotoku, J., Bando, T., DeLuca, E.E., Lundquist, L.L., Tsuneta, S., Harra, L.K., Katsukawa, Y., Kubo, M., Hara, H., Matsuzaki, K., Shimojo, M., Bookbinder, J.A., Golub, L., Korreck, K.E., Su, Y., Shibasaki, K., Shimizu, T., Nakatani, I.: 2007, *Science* **318**, 1585. DOI. ADS.
- Savcheva, A.S., van Ballegoijen, A.A., DeLuca, E.E.: 2012, *Astrophys. J.* **744**, 78. DOI. ADS.
- Scherrer, P.H., Bogart, R.S., Bush, R.I., Hoeksema, J.T., Kosovichev, A.G., Schou, J., Rosenberg, W., Springer, L., Tarbell, T.D., Title, A., Wolfson, C.J., Zayer, I., MDI Engineering Team: 1995, *Solar Phys.* **162**, 129. DOI.
- Schmieder, B., Mandrini, C.H., Démoulin, P., Aulanier, G., Li, H., Berlicki, A.: 2007, *Adv. Space Res.* **39**, 1840. DOI. ADS.
- Schrijver, C.J., Title, A.M.: 2002, *Solar Phys.* **207**, 223. DOI. ADS.
- Spoelstra, T.A.T., Kelder, H.: 1984, *Radio Sci.* **19**, 779. DOI. ADS.
- Stewart, R.T.: 1977, *Radiofizika* **20**, 1338. ADS.
- Suess, S.T.: 1979, *Space Sci. Rev.* **23**, 159. DOI. ADS.
- Suzuki, S., Dulk, G.A.: 1985, In: McLean, D.J., Labrum, N.R. (eds.) *Bursts of Type III and Type V*, Cambridge University Press, Cambridge, 289. ADS.
- Svestka, Z.: 1983, *Space Sci. Rev.* **35**, 259. DOI. ADS.
- Sweet, P.A.: 1958, In: Lenhart, B. (ed.) *IAU Symp. 6: Electromagnetic Phenomena in Cosmical Physics*, Cambridge University Press, Cambridge, 123. ADS.
- Titov, V.S., Mikić, Z., Linker, J.A., Lionello, R., Antiochos, S.K.: 2011, *Astrophys. J.* **731**, 111. DOI. ADS.
- Tóth, G., van der Holst, B., Huang, Z.: 2011, *Astrophys. J.* **732**, 102. DOI. ADS.
- Uchida, Y., McAllister, A., Strong, K.T., Ogawara, Y., Shimizu, T., Matsumoto, R., Hudson, H.S.: 1992, *Publ. Astron. Soc. Japan* **44**, L155. ADS.
- van Driel-Gesztelyi, L., Culhane, J.L., Baker, D., Démoulin, P., Mandrini, C.H., DeRosa, M.L., Rouillard, A.P., Opitz, A., Stenborg, G., Vourlidas, A., Brooks, D.H.: 2012, *Solar Phys.* **281**, 237. DOI. ADS.
- von Steiger, R., Geiss, J., Gloeckler, G.: 1997, In: Jokipii, J.R., Sonett, C.P., Giampapa, M.S. (eds.) *Cosmic Winds and the Heliosphere*, The Univ. Arizona Press, Tucson, 581. ADS.
- von Steiger, R., Zurbuchen, T.H., Geiss, J., Gloeckler, G., Fisk, L.A., Schwadron, N.A.: 2001, *Space Sci. Rev.* **97**, 123. DOI. ADS.
- Wang, Y.-M., Sheeley, N.R. Jr.: 1990, *Astrophys. J.* **365**, 372. DOI. ADS.
- Wang, Y.-M., Sheeley, N.R., Socker, D.G., Howard, R.A., Rich, N.B.: 2000, *J. Geophys. Res.* **105**, 25133. DOI. ADS.
- Wentzel, D.G.: 1986, *Solar Phys.* **103**, 141. DOI. ADS.
- Wilmot-Smith, A.L., Hornig, G.: 2011, *Astrophys. J.* **740**, 89. DOI. ADS.
- Wyper, P.F., Pontin, D.I.: 2013, *Phys. Plasmas* **20**(3), 032117. DOI. ADS.
- Zurbuchen, T.H., von Steiger, R.: 2006, In: Lacoste, H. (ed.) *SOHO-17. 10 Years of SOHO and Beyond SP-617*, ESA, Noordwijk, 7.1. ADS.
- Zurbuchen, T.H., Hefti, S., Fisk, L.A., Gloeckler, G., von Steiger, R.: 1999, *Space Sci. Rev.* **87**, 353. DOI. ADS.
- Zurbuchen, T.H., Fisk, L.A., Gloeckler, G., von Steiger, R.: 2002, *Geophys. Res. Lett.* **29**, 1352. DOI. ADS.